Time Statistics of Propagation over the Ocean Surface: A Numerical Study

Baran U. Ungan and Joel T. Johnson, *Member, IEEE*

***Abstract*—Temporal evolution of the ocean surface affects the received signal characteristics in a shipboard communication system. Predicting these time-varying properties is important in studying multipath fading problems. A statistical channel description to the second order is provided by knowledge of the coherent and incoherent power levels as well as the power spectrum of the received field. Several other time-dependent properties of a Gaussian channel can be determined from these statistics. In this paper, a method of moments (MoM) model for propagation over a one-dimensional (1-D) time-evolving, perfectly conducting rough surface is applied to numerically study time statistics of propagation over the ocean. The ocean surface is described by a Pierson-Moskowitz spectrum and evolves in time according to a linear hydrodynamic dispersion relation. Due to the large size of propagation geometries in terms of the electromagnetic wavelength, an efficient numerical method is required to complete the simulation in a reasonable time. The recently developed forward–backward method with a novel spectral acceleration (F-B/NSA) technique is applied and enables time-evolving simulations for many realizations to be calculated so that reasonable statistics are obtained. Numerically obtained results for the coherent and the incoherent powers are illustrated. These results are compared with available analytical approximations to investigate the success of the approximate methods. Particular emphasis is placed on comparison with the Kirchhoff approximation, which provides reasonable predictions for smoother surface profiles and larger grazing angles.**

***Index Terms*—Electromagnetic propagation, rough surface scattering, sea surface scattering.**

I. Introduction

A TEMPORALLY varying ocean surface imposes certain properties on the transmitted signal in a maritime communication link. Predicting the time statistics of the received signal is important in the characterization of the propagation channel. Knowledge of the coherent and incoherent power levels along with the power spectrum of the received signal provides a complete second order statistical description, and in the case of a Gaussian received field, i.e., the real and imaginary components of the field are independent Gaussian random processes, the second order statistics completely describe the time varying channel properties. Other time dependent properties of a Gaussian channel, such as the fade duration and the fade occurrence interval, can be determined from these statistics.

Although several theoretical and empirical models have been developed to describe some of these characteristics [1]–[6], approximations are required in their derivation and therefore limit their applicability. Due to the limitations of the analytical models, numerical techniques have been developed for the solution of the propagation over the ocean problem. However, typical profiles for microwave propagation over the ocean surface involve distances on the order of tens or hundreds of thousands of wavelengths separating the transmitting and receiving antennas. Such scattering geometries in terms of a wavelength are usually considered too large for exact numerical methods. Moreover, simulations of propagation over a time-varying ocean surface require repeated solutions of the scattering problem. Fortunately, efficient numerical techniques for rough surface scattering that allow propagation simulations for these size profiles to be performed [7]–[14] have recently been developed. One approximate technique, the parabolic wave equation method (PWE) [13], [14] is highly efficient for propagation studies and can include atmospheric effects such as ducting. However, it neglects the effects of small-scale surface roughness that can potentially be important in the prediction of propagation time statistics, especially at large grazing angles. Exact numerical methods based on the method of moments (MoM) solution are usually less efficient compared to the approximate methods. However, it has been shown that the exact MoM solution can be obtained in a relatively efficient manner using the forward–backward method with a novel spectral acceleration (F-B/NSA) technique [10].

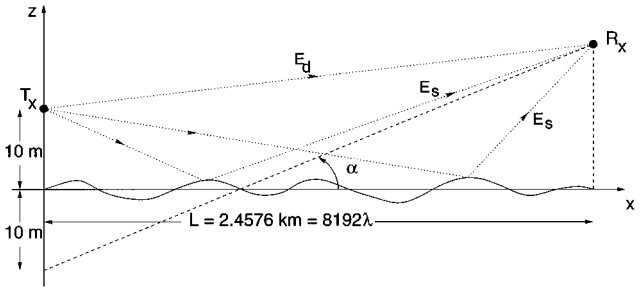

Fig. 1. Geometry of the propagation problem.

In this paper, scattering of electromagnetic waves from a time evolving rough ocean surface is studied. The operating frequency is selected to be 1 GHz, a typical UHF band frequency used in shipboard communication systems. Atmospheric effects such as ducting and scintillations are neglected for simplicity. The geometry of the problem is shown in Fig. 1. Both the transmitting and the receiving antennas are chosen to be horizontally polarized line sources. The transmitter height is fixed at 10 m above the mean surface level. Variations of the receiver height are described in terms of the grazing angle α measured

Manuscript received September 3, 1999; revised March 8, 2000.

The authors are with the Department of Electrical Engineering and ElectroScience Laboratory, The Ohio State University, Columbus, OH 43210 USA (e-mail: johnson@ee.eng.ohio-state.edu).

Publisher Item Identifier S 0196-2892(00)05894-0.

through the mirror image of the transmitter (see Fig. 1). The horizontal distance L separating the two antennas is on the order of kilometers, while the antenna heights are on the order of meters. Therefore, propagation is close to grazing, and it is reasonable to model the ocean surface as a one-dimensional (1-D) perfectly electric conducting (PEC) boundary.

As shown in Fig. 1, the total received electric field can be decomposed into two components: the direct field E_d, which would be received in free space without considering the surface, and the scattered field E_s, which is radiated from the induced currents on the surface. Since the total field at the receiver is the sum of these two, there is a possibility for them to interfere with each other, causing multipath fading effects. Due to the roughness of the ocean surface, the scattered field path is not unique, resulting in irregular multipath fading statistics. Usually, it is convenient to express the received signal in terms of the propagation gain, defined as

$$F = \frac{E_d + E_s}{E_d} \tag{1}$$

which is the ratio of the total field to the direct field. In the following, the propagation gain F will be used to present the characteristics of the received signal.

Accurately modeling the ocean surface is important in the prediction of realistic time statistics of the received signal. A detailed description of surface models used in numerical simulations and analytical calculations is given in Section II. Temporal variations of the surface and resulting changes in the fields are also discussed in this section. Coherent and incoherent components of the received power are studied in Section III. The power spectrum of the signal is investigated in Section IV. Numerically obtained results for these quantities are compared with available analytical approximations to assess the success of the approximate methods. Particular emphasis is placed on comparison with the Kirchhoff approach, which is shown to provide reasonable predictions in many cases for the near-forward propagation geometries. A discussion of propagation channel properties and several other time statistics of the received field derived from the second-order statistics is given in Section V. Finally, conclusions are presented in Section VI.

II. Time Variation of the Ocean Surface

Numerical and analytical calculations of the received time-varying fields over the ocean surface demand several characteristics of the surface to be known. Time variations of the propagation geometry are handled by discretizing the time duration into a number of time steps. Then, time-varying fields are obtained by solving the scattering problem "frozen" at each time step as described for backscattering in [16]. Finally, the time statistics are determined by averaging these field quantities over several realizations of the surface. This procedure requires statistics of each point on the ocean surface as a random variable, the spectrum (or the correlation function) of the surface, and the hydrodynamic relation with which it evolves in time.

In this paper, the ocean surface is modeled as a Gaussian random process with a Pierson–Moskowitz spectrum. The

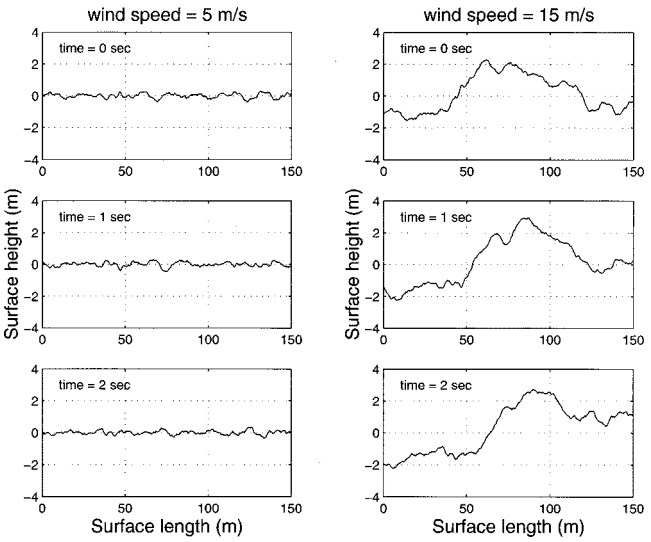

Fig. 2. Time variation of a single realization of the ocean surface for wind speeds 5 m/s and 15 m/s.

Pierson-Moskowitz spectrum is defined in terms of the spatial wavenumber k of the surface as [15], [16]

$$\Psi(k) = \frac{\alpha}{4|k|^3}\, e^{-(\beta g^2/u^4 k^2)} \tag{2}$$

where $\alpha = 0.0081$ and $\beta = 0.74$ are two empirical constants, $g = 9.81$ m/s^2 is the gravitational acceleration constant, and u is the wind speed measured in m/s. Thus, the spectrum is dependent on the wind speed such that higher wind speeds cause low frequency components of the surface to have larger amplitudes. Temporal evolution of the ocean surface is modeled according to the linear gravity/capillary wave dispersion relation for deep-water, given in terms of the phase velocity of each frequency component as [16]

$$v_p = \sqrt{g/k + \kappa k} \tag{3}$$

where g is the gravitational acceleration constant and $\kappa = 7.4 \times 10^{-5}$m^3/s^2 accounts for the surface tension. While nonlinear models for hydrodynamics of the ocean surface are available, they are extremely computationally expensive. The linear propagation model used here avoids this computational complexity while still retaining many of the basic features of sea surface temporal evolution. Numerically generated temporal evolution of the ocean surface is as shown in Fig. 2 for wind speeds 5 m/s and 15 m/s. It can be seen from the figure that higher wind speeds result in larger waves with larger wavelengths. Phase velocities of the surface waves range from 0.5 m/s to 7 m/s for a wind speed of 5 m/s and to 18 m/s for a wind speed of 15 m/s.

Time variation of the scattering geometry modulates the received signal. Therefore, a transmitted continuous wave signal is received as a time-varying propagation gain that can be expressed as

$$F(t) = Re\{A(t)e^{j\phi(t)}e^{j\omega t}\} \tag{4}$$

where $A(t)$ and $\phi(t)$ are the time-dependent amplitude and phase of the envelope of F, respectively. The carrier frequency

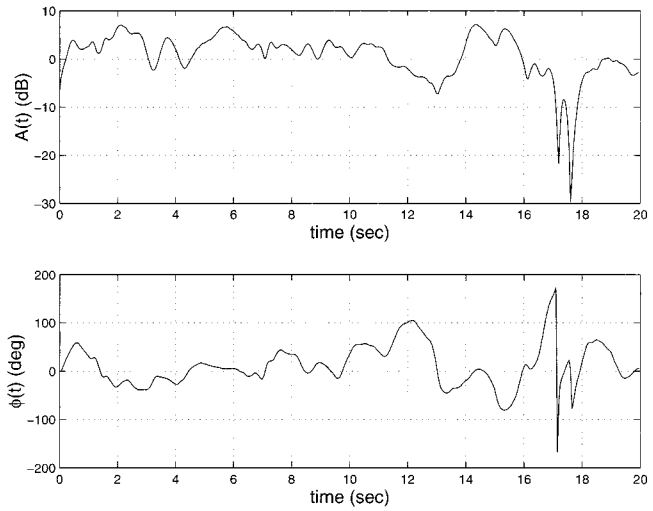

Fig. 3. Time variation of the magnitude $A(t)$ and the phase $\phi(t)$ of a single realization of the propagation gain $F(t)$ (wind speed = 15 m/s and $\alpha = 4.88^{\circ}$).

$f = 1$ GHz is included in (4) through the angular frequency $\omega = 2\pi f$. The time-varying propagation gain is computed numerically using the F-B/NSA technique at each frozen time step. Computing the received field at one time step involves the numerical solution of the scattering from the rough ocean surface of length $L = 2.4576$ km discretized into 32 768 points with $\lambda 4$ increments, where λ is the electromagnetic wavelength. The F-B/NSA method takes approximately 3 min and five iterations to simulate one time step for the 5 m/s wind speed and 4.5 min and six iterations for the 15 m/s wind speed on a 200 MHz Pentium Pro processor. A single realization of $F(t)$ generated from 400 time steps separated by a time increment of $\Delta t = 0.05$ s at a grazing angle of $\alpha = 4.88^{\circ}$ and a wind speed of 15 m/s is shown in Fig. 3. The duration of the time increments is chosen to maintain the continuity of the consecutive realizations and thus, a smooth evolution of both the ocean surface and the fields is observed. Note the significant variations in amplitude and phase occurring in this example. These time-varying properties broaden the frequency spectrum of the received field around the carrier frequency, as described in more detail in Section IV. Fig. 3 also displays a typical fade between 17 and 18 s, caused by interference between the large number of ray paths occuring at high grazing angles for a rough surface profile. A statistical description of these fading characteristics is given in Section V.

III. Coherent and Incoherent Powers

Since the ocean surface is described statistically as a random process, the received signal is a random variable. Therefore, ensemble averages and time averages of the field and power quantities are considered in calculations. Ensemble averages are mean values for different realizations of the ocean surface, each of which is generated as a sample of the random process describing the surface. Time averages, however, are averages over a specified time duration. Since ocean surface realizations at a specific time are correlated to those at an earlier time, time averages are different from ensemble averages for a limited time duration.

It is convenient to separate the propagation gain F into its coherent and incoherent components. The coherent component is the power of average field F, and it is expressed as $P_C = |\langle F \rangle|^2$. Due to the averaging operation that cancels the random variations in F, the coherent power depends mainly on the large scale geometry of the problem. The incoherent component is the mean of the variance of F, and it is expressed as $P_I = \langle |F - \langle F \rangle|^2 \rangle$. In these definitions, $\langle \cdot \rangle$ denotes the ensemble average (or arithmetic mean) over many realizations. Since the variance describes how a function is spread around the mean, the incoherent power corresponds to the amount of deviation from the coherent component (i.e., it is a measure of the randomness of the received power). In the rough surface scattering problem, the incoherent power depends on the random variations of the surface. Accordingly, the coherent component is dominant for a smooth surface profile, whereas the incoherent component can be dominant for a rough surface profile.

The coherent and incoherent powers are numerically generated using the F-B/NSA method and by ensemble averaging over 50 realizations of the ocean surface at a fixed time (say $t = 0$). The simulation results of the coherent and incoherent power as a function of the grazing angle α are given in Figs. 4 and 5 for wind speeds 5 m/s and 15 m/s. The low wind speed case for the coherent power shows the characteristic multipath fading pattern clearly, due to the interference between the direct and specularly reflected wave. In the high wind speed case, however, the rough surface profile causes a reduction in the specular reflection coefficient so that the coherent power vanishes for large grazing angles. This is due to the increased randomness in the received field, which in turn results in a larger incoherent power.

Monte Carlo-averaged MoM results are compared with a Monte Carlo physical optics (PO) method. Monte Carlo PO results are generated using the Kirchhoff approach (i.e., tangent plane approximation) applied to determine induced currents at each point on the surface, and ensemble averaging over 50 realizations of scattered fields. Since the Kirchhoff approach does not take into account shadowing and multiple scattering effects, the scattered field component of the received field is multiplied by a shadowing factor in order to improve the results. The shadowing factor for forward scattering is given as [17]

$$S(\alpha) = \frac{1}{2\Lambda(\alpha) + 1} \tag{5}$$

and

$$\Lambda(\alpha) = \frac{1}{2}\left[\sqrt{\frac{2s^2}{\pi}}\,\frac{1}{\tan\alpha}\,e^{-\tan^2\alpha/2s^2} - \operatorname{erfc}\left(\frac{\tan\alpha}{\sqrt{2s^2}}\right)\right] \tag{6}$$

where s^2 is the mean square surface slope, erfc$(\cdot)$ is the complementary error function, and α is the grazing angle. This shadowing factor, however, applies only under the assumption that the received field is dominated by its incoherent component. Therefore, it is only applied to the calculation of the incoherent power. Monte Carlo PO simulations for the coherent and the incoherent power are also given in Figs. 4 and 5. It is clear that

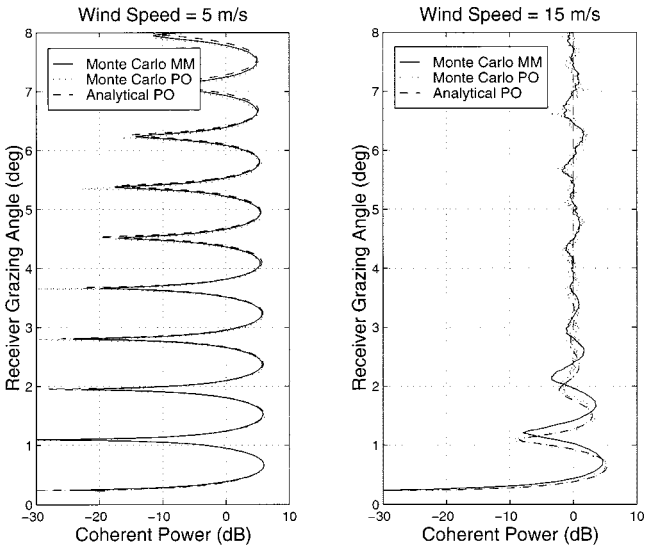

Fig. 4. Coherent power as a function of the grazing angle for wind speeds 5 m/s and 15 m/s.

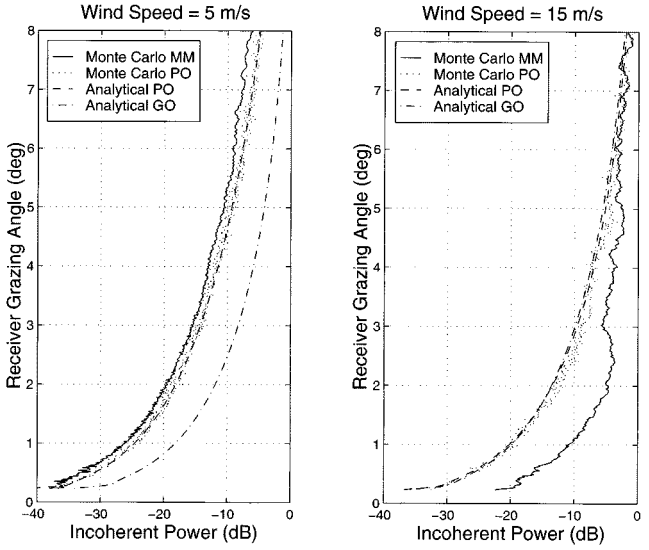

Fig. 5. Incoherent power as a function of the grazing angle for wind speed 5 m/s and 15 m/s.

both MoM and PO results are in very good agreement for the low wind speed case. At high wind speeds, however, for low grazing angles, the incoherent power numerical PO results deviate from the exact MoM solution. This is due to the relatively more complex scattering mechanisms involved for rough surfaces near grazing for which the tangent plane approximation may not be valid. Note also the shifted locations of the first few peaks and nulls in the coherent power pattern in the 15 m/s wind speed case, in which PO fails to follow the exact solution. These results appear to describe a difference in the coherent reflection coefficient from that obtained in the PO approximation, however an analytical description of this effect has yet to be obtained.

In addition to the Monte Carlo computation of the coherent and incoherent powers with the MoM and PO, analytical techniques are also applied to determine these quantities. The coherent component of the received power corresponding to an ensemble average is calculated through the use of the reduced reflection coefficient on a flat surface. This modified field reflection coefficient takes into account the surface roughness effects and is derived using the Kirchhoff approximation as [17]

$$R_r = Re^{-2k^2\sigma^2 \sin^2 \alpha} \tag{7}$$

where R is the reflection coefficient at the boundary, which equals -1 for the PEC surface considered in this paper, k is the electromagnetic wavenumber $2\pi\,\lambda$, and σ^2 is the variance of the surface height profile. Results for coherent power using this approach are given in Fig. 4 for two wind speeds. For low wind speeds, the analytical PO approach is observed to be satisfactory, whereas for high wind speeds, it follows the numerical PO results instead of the exact MoM solution. Also note the effects of the rapidly decaying reflection coefficient as the grazing angle increases for the rougher surface.

The Kirchhoff approach is also applied to calculate the ensemble average incoherent power. The procedure leading to the incoherent power expression is outlined in the Appendix. The incoherent power results of the expression in (28) of the Appendix are given in Fig. 5. Analytically derived PO results [which also include the shadowing effect correction function of (5) and (6)] are in good agreement with the numerical PO solution. Both methods closely approximate the exact MoM results for smoother surfaces but fail to predict the exact results for rougher surfaces at near grazing angles.

Another analytical method to test against the numerical simulation results is the geometrical optics (GO) approach, which is the large surface height limit of the PO approximation. For large surface profiles, such that $k_{dz}\sigma \gg 1$, it can be shown that $D_{L/N}$ in (30) of the Appendix takes the form

$$D_{L/N} = \sqrt{\frac{2\pi}{k_{dz}^2\sigma^2}}\; e^{-(k_{dx}^2/2k_{dz}^2 s^2)}. \tag{8}$$

The incoherent power results obtained by the GO limit are given in Fig. 5. As expected, the GO results follow the PO approximations for rougher surfaces corresponding to large wind speeds ($k\sigma = 25.45$ at 15 m/s wind speed) and deviate from PO for smoother profiles ($k\sigma = 2.83$ at 5 m/s wind speed).

As a conclusion, the PO approximation predicts the coherent and the incoherent power characteristics accurately except in some limiting cases. It is shown that for smoother surfaces and large grazing angles, the PO results are in reasonable agreement with the numerical simulations. However, when the surface scattering mechanism is too complicated to be approximated by the tangent plane approach, the PO solution is shown to underestimate the incoherent power level by as much as 10 dB.

IV. Power Spectrum

The power spectrum of the received signal, along with the coherent and incoherent power levels, provides a complete second-order statistical description of the received field. In the case of a continuous wave transmitted signal, the received signal is modulated due to the temporally evolving ocean surface. The power spectrum is the measure of the frequency modulation introduced by the time-varying surface and is dependent on the wind speed

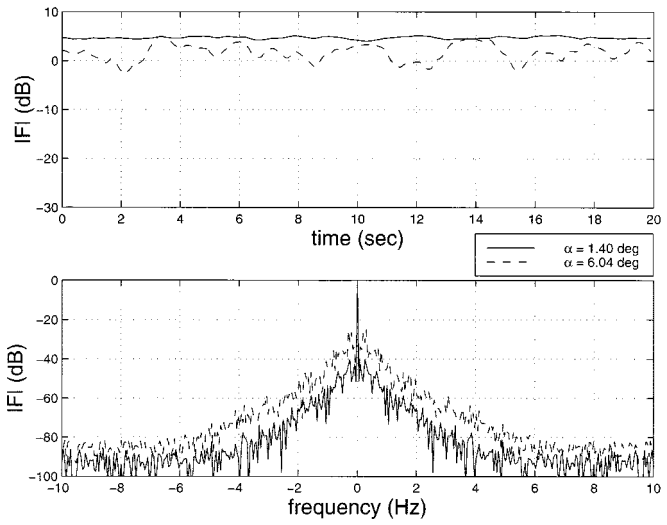

Fig. 6. Propagation gain F as a function of time and frequency for grazing angles of 1.40° and 6.04° (wind speed = 5 m/s).

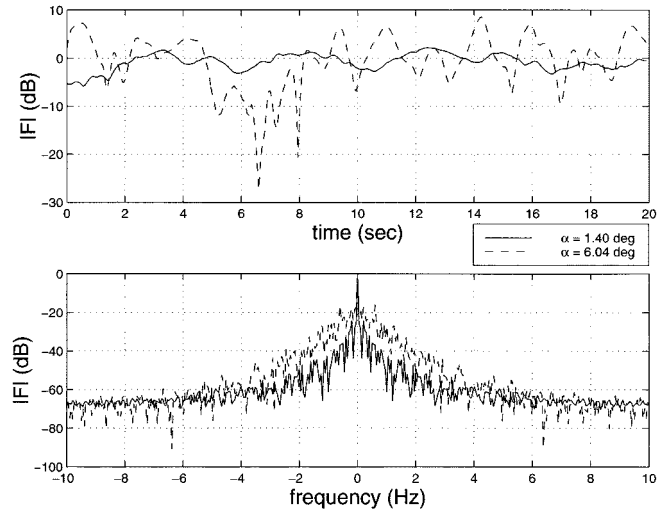

Fig. 7. Propagation gain F as a function of time and frequency for grazing angles of 1.40° and 6.04° (wind speed = 15 m/s).

and the grazing angle. In order to demonstrate the effects of these parameters on the spectrum, the amplitude of the propagation gain F for one realization is shown in both time domain and frequency domain in Figs. 6 and 7. It is clear that an increase in randomness of the received field (either by a larger wind speed or a larger grazing angle) results in a broader spectrum.

The power spectrum is defined as the Fourier transform of the incoherent correlation function

$$\Gamma_I(\tau) = \langle (F(t) - \langle F(t) \rangle)(F(t+\tau) - \langle F(t+\tau) \rangle)^* \rangle \quad (9)$$

where the inner brackets ($\langle \cdot \rangle$) denote time averages, and the outer brackets denote both ensemble and time averages. Note that according to the definition of $F(t)$ given in (4), the carrier frequency is factored out in the resulting power spectrum expression. Therefore, it should be remembered that the spectrum is centered around the carrier frequency. It is also worth noting

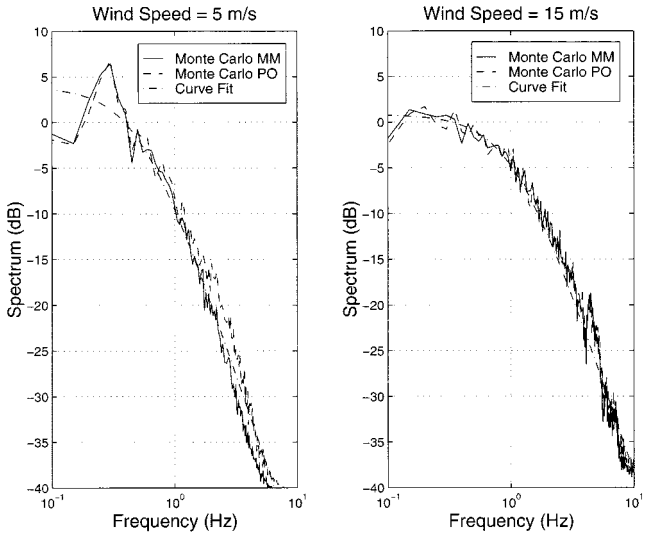

Fig. 8. Power spectrum for wind speeds 5 m/s and 15 m/s.

that the peak magnitude is determined by the incoherent power level. This peak value is removed and the power spectrum results presented in this section are normalized so that the area under them is equal to unity.

The power spectra are numerically generated using the F-B/NSA method. Monte Carlo results are produced by performing time averages in (9) over 400 time steps of total duration 20 s to obtain the incoherent correlation function, then the resultant spectra are ensemble averaged over 20 realizations at a grazing angle of 7.19°. The results of this operation are presented in Fig. 8 for two different wind speeds, together with the numerical PO results obtained in a similar way using the Kirchhoff approach instead of the exact solution. It is observed that these two methods yield similar results, even when the incoherent power level is underestimated by the PO approximation. It is also of interest to examine closely the effect of the dominant wave structure. For the 5 m/s wind speed case, the dominant wave has a wavenumber of about 0.2 rad/s and according to the dispersion relation, moves with a phase velocity of about 7 m/s, thus creating a peak in the spectrum at 0.22 Hz, as observed in Fig. 8. Similarly, the peak for the 15 m/s wind speed case occurs at 0.09 Hz (not resolved for the results presented).

As described in Section II, the ocean surface evolves in time according to the hydrodynamic dispersion relation given in (3), which requires each frequency component of the surface profile to move with a different phase velocity. Due to these dispersive properties of the ocean surface, it is difficult to obtain an analytical description for the power spectrum of the received field. Several analytical and empirical models to assign an approximate random velocity to the ocean surface [2], [3], [18] are found to be unsatisfactory upon comparison with the numerical simulations. Therefore, the numerically generated spectra are matched by curve fitting. It has been found that a power spectrum model of the form

$$W(f) = \frac{4/(\pi f_0)}{(1 + (f/f_0)^2)^2} \quad (10)$$

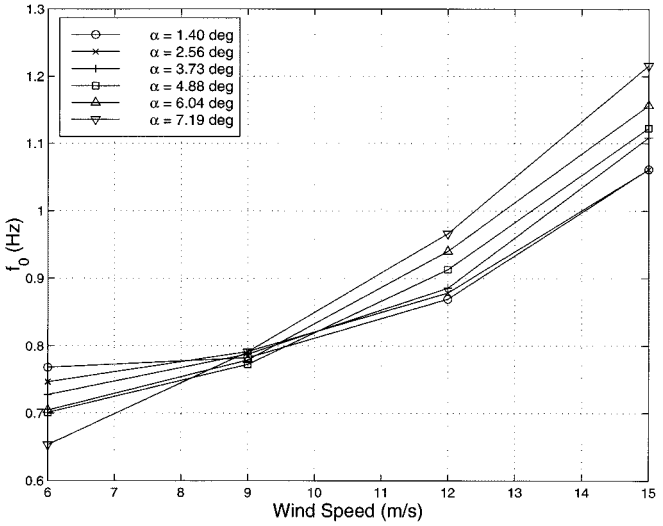

Fig. 9. Cutoff frequency f_0 as a function of wind speed and grazing angle α.

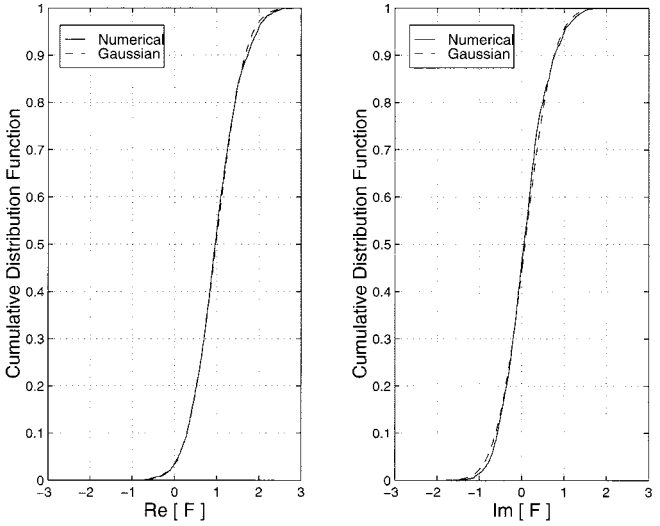

Fig. 10. Cumulative distribution functions of the real and imaginary parts of the propagation gain F. Numerical simulations are compared with the Gaussian CDF for wind speed $=$ 15 m/s and grazing angle $=$ 6.04°.

can be used to fit the numerical results reasonably. The function $W(f)$ has a single parameter f_0, which corresponds to the -6 dB bandwidth of the spectrum. Curve fitting results are also presented in Fig. 8. As with the spectrum itself, the cutoff frequency f_0 varies with wind speed and grazing angle α. As shown in Fig. 9, f_0 depends strongly on the wind speed and increases as wind speed increases, whereas it depends rather weakly on the grazing angle and does not display a proportional variation.

As a conclusion, the numerical PO approximation predicts the frequency domain characteristics of the received field very accurately. Although an analytical approximation to the power spectrum is not available, the empirical curve fitting approach presented above is shown to reproduce the numerical results reasonably.

V. Other Time Statistics

As discussed in the previous sections, the second-order time statistics of the received signal are determined by the coherent and incoherent power levels and the power spectrum. In the case of a Gaussian channel, the real and imaginary parts of the received field are independent Gaussian random processes and time statistics of the second order give a complete description of the received signal characteristics.

In order to investigate the nature of the propagation channel discussed in this paper, histograms of the received field are generated numerically from five realizations of the ocean surface, each of which evolves in time for 400 time steps. It is observed that the real and the imaginary parts of the propagation gain F indeed approximate Gaussian random variables with variance equal to the incoherent power level, as shown in Fig. 10. Moreover, the correlation coefficient of the real and imaginary parts is found to be less than 0.1, which suggests that they are independent random variables. Therefore, it is reasonable to assume that the propagation channel is Gaussian under the assumption of the ocean surface models used here.

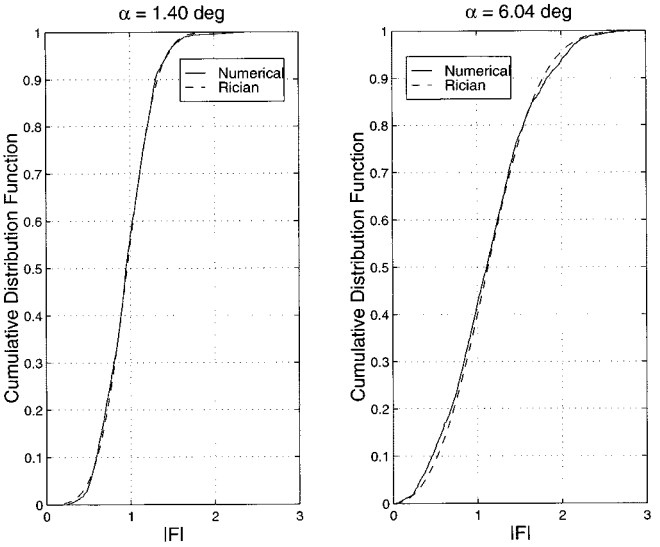

Fig. 11. Cumulative distribution function of the magnitude of the propagation gain F. Numerical simulations are compared with the Rician CDF for wind speed $=$ 15 m/s and grazing angles 1.40° and 6.04°.

A study of the magnitude distribution of the propagation gain shows that it can be approximated by the Rician density function [1]

$$f(F) = \frac{2F}{P_I}\ \exp\left(-\frac{F^2 + P_C}{P_I}\right) I_0\left(\frac{2F\sqrt{P_C}}{P_I}\right) \qquad (11)$$

where P_C and P_I are the coherent and incoherent components, respectively, of the power in the scattered field. $I_0(\cdot)$ is the zeroth order modified Bessel function of the first kind. A comparison of the cumulative distribution function of the magnitude of F, generated numerically from 2000 samples, and the Rician distribution is given in Fig. 11. It is worth noting that for the limiting case of a highly random field (i.e., a zero coherent field and an incoherent field equal to the mean power), the Rician density function of (11) reduces to the Rayleigh density function.

Since the complete statistical description of the propagation channel is known, it is possible to obtain other time statistics from the second-order statistics described in this paper. For example, the fade duration statistics and the fade occurrence interval can be predicted from the power spectrum of the received fields, as discussed in detail in [2].

VI. Conclusions

A numerical study of the time statistics of the received signal in a maritime communication system is presented. It is shown that the time statistics of second order can be produced by numerical methods. PO and GO approximations are tested against the results of these numerical methods and are found to predict the simulated results of the coherent and incoherent power levels for some limited cases. It is observed that the PO approximation matches the exact numerical model for smoother surfaces (corresponding to lower wind speeds) or larger grazing angles, whereas the GO approximation can only reproduce the PO results for large surface height profiles. It is shown that the numerical PO approximation predicts the spectral characteristics of the signal at the receiver very accurately. An analytical model for the power spectrum of received fields is difficult to realize since the time evolution of the ocean surface is dispersive. However, an empirical function is shown to match the modeled spectra well. These statistics can be used to obtain other characteristics of the propagation channel such as the field density and distribution functions, fade duration, and fade occurrence interval. Results produced in this paper can be applied to study multipath fading problems in ocean communication systems.

Appendix
Calculating the Ensemble Average Incoherent Power

The ensemble average incoherent power is derived using the Kirchhoff approach as follows. Consider a line source transmitter located at $\overline{r_t} = \hat{x}x_t + \hat{z}z_t$ for which the incident field is expressed as

$$\overline{E_i}(\overline{r}) = \hat{y}\,\frac{E_0}{\pi}\int_{-\infty}^{+\infty} \cdot \frac{\exp[-j(k_{xi}(x-x_t)-k_{zi}(z-z_t))]}{k_{zi}}\,dk_{xi} \quad (12)$$

where $k_{zi} = \sqrt{k^2 - k_{xi}^2}$, and the corresponding direct and scattered fields reaching the receiver located at $\overline{r_r} = \hat{x}x_r + \hat{z}z_r$ are

$$\overline{E_d}(\overline{r}) = \hat{y}\,\frac{E_0}{\pi}\int_{-\infty}^{+\infty} \cdot \frac{\exp[-j(k_{xi}(x_r-x_t)-k_{zi}(z_r-z_t)]}{k_{zi}}\,dk_{xi} \quad (13)$$

$$= E_0 H_0^{(2)}(k|\overline{r_r} - \overline{r_t}|) \quad (14)$$

and

$$\overline{E_s}(\overline{r}) = -\hat{y}\,\frac{E_0}{2\pi^2}\int_{-\infty}^{+\infty}\frac{e^{-j\overline{k_s}\cdot\overline{r_r}}}{k_{zs}} \cdot \int_{-\infty}^{+\infty}\frac{e^{-j\overline{k_i}\cdot\overline{r_t}}}{k_{zi}}\,G(\overline{k_i},\overline{k_s})\,dk_{xi}\,dk_{xs} \quad (15)$$

respectively, where $k_{zs} = \sqrt{k^2 - k_{xs}^2}$. In the above equations, $\overline{k_i} = \hat{x}k_{xi} - \hat{z}k_{zi} = \hat{x}k\sin\theta_i - \hat{z}\,k\cos\theta_i$ and $\overline{k_s} = \hat{x}k_{xs} + \hat{z}k_{zs} = \hat{x}k\sin\theta_s + \hat{z}k\cos\theta_s$ are the incident and scattered wave directions with θ_i and θ_s the incident and scattering angles. The function $G(\overline{k_i},\overline{k_s})$ in (15) is given by

$$G(\overline{k_i},\overline{k_s}) = \int_L e^{-j\overline{k_d}\cdot\overline{r'}}(k_{xi}f'(x') - k_{zi})\,dx' \quad (16)$$

where $\overline{k_d} = \overline{k_i} - \overline{k_s}$. The ocean surface profile, as a function of the horizontal position x, is denoted as $f(x)$, and its derivative with respect to x is denoted as $f'(x)$. Rewriting (15) and (16) in terms of the angles θ_i and θ_s yields

$$\overline{E_s}(\overline{r}) = -\hat{y}\,\frac{E_0 k}{2\pi^2}\int_{C_s}\exp[-jk(r_x\sin\theta_s + r_z\cos\theta_s)] \cdot \int_{C_i}\exp[+jk(t_x\sin\theta_i - t_z\cos\theta_i)] \cdot G(\theta_i,\theta_s)\,d\theta_i\,d\theta_s \quad (17)$$

and

$$G(\theta_i,\theta_s) = \int_L \exp[-jk[(\sin\theta_i - \sin\theta_s)x' - (\cos\theta_i + \cos\theta_s)f'(x')]] \cdot (f'(x')\sin\theta_i + \cos\theta_i)\,dx' \quad (18)$$

where C_i and C_s are the integration paths in the complex plane corresponding to the change of variables $k_{xi,s} = k\sin\theta_{i,s}$. Changing the order of integration in (17) gives

$$\overline{E_s}(\overline{r}) = -\hat{y}\frac{E_0 k}{2\pi^2}\int_L\left[\int_{C_i}\exp[-jk[(x'-t_x)\sin\theta_i + (t_z - f(x'))\cos\theta_i](f'(x')\sin\theta_i + \cos\theta_i)\,d\theta_i\right] \cdot \left[\int_{C_s}\exp[-jk[(r_x - x')\sin\theta_s + (r_z - f(x'))\cos\theta_s]\,d\theta_s\right]dx' \quad (19)$$

The scattered field expression in (19) involves two angular integrals and another integral along the surface profile. In order to simplify this expression for practical use, some approximations are needed. First, the outer integral is separated into a number of finite segments. These segments along the surface need to be small enough to maintain a reasonable continuity in local incident and scattered angles but must also be large enough so that fields scattered from each segment are uncorrelated with those from neighboring segments. It has been observed that a segment size of about 20 m is sufficient for the examples illustrated. The resulting expression for the scattering field is

$$\overline{E_s}(\overline{r}) = -\hat{y}\frac{E_0 k}{2\pi^2}\sum_{n=1}^{N}\int_{L/N}\left[\int_{C_i}\exp[-jk[(x'_n - t_x)\sin\theta_{in} + (t_z - f(x'_n))\cos\theta_{in}]] \cdot (f'(x'_n)\sin\theta_{in} + \cos\theta_{in})\,d\theta_{in}\right] \cdot \left[\int_{C_s}\exp[-jk[(r_x - x'_n)\sin\theta_{sn} + (r_z - f(x'_n))\cos\theta_{sn}]]\,d\theta_s\right]dx'_n \quad (20)$$

where N is the number of segments along the propagation distance L. Next, the angular integrals are approximated using the stationary phase method assuming the incident and scattering angles do not change much within each segment. Hence

$$\int_{C_i} \exp[-jk[(x'_n - t_x)\sin\theta_{in} + (t_z - f(x'_n))\cos\theta_{in}]] \cdot (f'(x'_n)\sin\theta_{in} + \cos\theta_{in})\, d\theta_{in} \approx \sqrt{\frac{2\pi j}{k}} \cdot \frac{\exp[-jk[(x'_n - t_x)\sin\theta^s_{in} + (t_z - f(x'_n))\cos\theta^s_{in}]]}{[(x'_n - t_x)^2 + t_z^2]^{1/4}} \cdot (f'(x'_n)\sin\theta^s_{in} + \cos\theta^s_{in}) \tag{21}$$

and

$$\int_{C_s} \exp[-jk[(r_x - x'_n)\sin\theta_{sn} + (r_z - f(x'_n))\cos\theta_{sn}]]\, d\theta_{sn} \approx \sqrt{\frac{2\pi j}{k}} \cdot \frac{\exp[-jk[(r_x - x'_n)\sin\theta^s_{sn} + (r_z - f(x'_n))\cos\theta^s_{sn}]]}{[(r_x - x'_n)^2 + r_z^2]^{1/4}}. \tag{22}$$

In the above equations, the x_n's are the center point of each segment along the x-axis, and θ^s_{in} and θ^s_{sn} are the incident and scattering angles at each segment center point. Inserting the above expressions in the scattered field integral results in

$$\overline{E_s}(\overline{r}) = -\hat{y}\frac{jE_0}{\pi}\sum_{n=1}^{N} \frac{\exp[-jk(-t_x\sin\theta^s_{in} + t_z\cos\theta^s_{in})]}{[(x'_n - t_x)^2 + t_z^2]^{1/4}} \cdot \frac{\exp[-jk(r_x\sin\theta^s_{sn} + r_z\cos\theta^s_{sn})]}{[(r_x - x'_n)^2 + r_z^2]^{1/4}} G_{L/N}(\theta^s_{in}, \theta^s_{sn}) \tag{23}$$

where

$$G_{L/N}(\theta^s_{in}, \theta^s_{sn}) = \int_{L/N} \exp[-jk[(\sin\theta^s_{in} - \sin\theta^s_{sn})x' - (\cos\theta^s_{in} + \cos\theta^s_{sn})f(x')]] \cdot (f'(x'_n)\sin\theta^s_{in} + \cos\theta^s_{in})\, dx'. \tag{24}$$

Integrating (24) by parts yields a simpler expression for $G_{L/N}(\theta^s_{in}, \theta^s_{sn})$

$$G_{L/N}(\theta^s_{in}, \theta^s_{sn}) = \left[\frac{1 + \cos(\theta^s_{in} + \theta^s_{sn})}{\cos\theta^s_{in} + \cos\theta^s_{sn}}\right] I_{L/N}(\theta^s_{in}, \theta^s_{sn}) \tag{25}$$

with

$$I_{L/N}(\theta^s_{in}, \theta^s_{sn}) = \int_{L/N} \exp[-jk[(\sin\theta^s_{in} - \sin\theta^s_{sn})x' - (\cos\theta^s_{in} + \cos\theta^s_{sn})f(x')]]\, dx'. \tag{26}$$

Finally, the incoherent component of the received field is calculated from the scattered field expression of (23). Since each segment of the surface is uncorrelated with the rest, the incoherent powers resulting from each segment can be added to give the total incoherent power. Therefore

$$P_I = \langle |F - \langle F\rangle|^2\rangle = \frac{\langle |E_s - \langle E_s\rangle|^2\rangle}{|E_d|^2} \tag{27}$$

$$= \frac{|E_0|^2}{\pi^2|E_d|^2}\sum_{n=1}^{N}[(x'_n - t_x)^2 + t_z^2]^{-(1/2)} \cdot [(r_x - x'_n)^2 + r_z^2]^{-(1/2)} \cdot \left[\frac{1 + \cos(\theta^s_{in} + \theta^s_{sn})}{\cos\theta^s_{in} + \cos\theta^s_{sn}}\right]^2 D_{L/N}. \tag{28}$$

The function $D_{L/N}$ is derived in [17] as

$$D_{L/N} = \langle |I_{L/N}|^2\rangle - |\langle I_{L/N}\rangle|^2 \tag{29}$$

$$= 2\int_{L/N}\left(\frac{L}{N} - x\right)(e^{-\sigma^2 k_{dz}^2(1 - C(x))} - e^{-\sigma^2 k_{dz}^2})\cos(k_{dx}x)\, dx \tag{30}$$

where $k_{dx} = k(\sin\theta^s_{in} - \sin\theta^s_{sn})$ and $k_{dz} = k(\cos\theta^s_{in} + \cos\theta^s_{sn})$. The correlation function of the ocean surface is denoted as $C(x)$ and is related to the inverse Fourier transform of the spectrum given in (2), such that $C(x) = (1/\sigma^2)F^{-1}\{\Psi(k)\}$. Since an analytical expression for the correlation function is not available in closed form, $C(x)$ is computed numerically using an inverse Fourier transform routine from the Pierson-Moskowitz spectrum. Equation (30) is evaluated numerically for every incident and scattering angle and takes considerably less time compared to Monte Carlo MoM and PO computations.

REFERENCES

[1] Y. Karasawa and T. Shiokawa, "Characteristics of L-band multipth fading due to sea surface reflection," *IEEE Trans. Antennas Propagat.*, vol. AP-32, pp. 618–623, 1984.

[2] ——, "Fade duration statistics of L-band multipath fading due to sea surface reflection," *IEEE Trans. Antennas Propagat.*, vol. AP-35, pp. 956–961, 1987.

[3] ——, "Spectrum of L-band multipath fading due to sea surface reflection," *Trans. IECE Jpn.*, vol. J67-B, no. 2, pp. 171–178, 1984.

[4] D. E. Maurer, "Forward scattering of electromagnetic energy from rough sea surfaces," *J. Geophys. Res.*, vol. 95, pp. 9689–9699, 1990.

[5] V. V. Chernukhov and V. D. Dobykin, "Bistatic radar wave scattering by sea surface," *J. Comm. Technol. Elec.*, vol. 40, pp. 70–77, 1995.

[6] P. Sobieski, A. Guissard, C. Baufays, and P. Siraut, "Sea surface scattering calculations in maritime satellite communications," *IEEE Trans. Commun.*, vol. 41, pp. 1525–1533, 1993.

[7] L. Tsang, C. H. Chan, K. Pak, and H. Sangani, "Monte Carlo simulations of large scale problems of random rough surface scattering and applications to grazing incidence with the BMIA/canonical grid method," *IEEE Trans. Antennas Propagat.*, vol. 43, pp. 851–859, 1995.

[8] J. T. Johnson, "On the canonical grid method for two-dimensional scattering problems," *IEEE Trans. Antennas Propagat.*, vol. 46, pp. 297–302, 1998.

[9] R. J. Burkholder and D.-H. Kwon, "High-frequency asymptotic acceleration of the fast multipole method," *Radio Sci.*, vol. 31, pp. 1199–1206, 1996.

[10] H.-T. Chou and J. T. Johnson, "Novel acceleration algorithm for the computation of scattering from rough surfaces with the forward-backward method," *Radio Sci.*, vol. 33, pp. 1277–1287, 1998.

[11] D. M. Milder, H. T. Sharp, and R. A. Smith, "Numerical simulation of ultra-wideband microwave backscatter from the wind roughened sea surface," Tech. Rep. AU-94-005, Arete Associates, Sherman Oaks, CA, 1994.
[12] P. J. Kaczkowski and E. I. Thorsos, "Application of the operator expansion method to scattering from one-dimensional moderately rough Dirichlete random surfaces," *J. Acoust. Soc. Amer.*, vol. 96, p. 457, 1994.
[13] A. E. Barrios, "Terrain modeling using the split-step parabolic equation method," in *Proc. Radar '92, IEE Conf. Pub.*, 1992, pp. 66–69.
[14] M. F. Levy, "Horizontal parabolic equation solution of radiowave propagation problems on large domains," *IEEE Trans. Antennas Propagat.*, vol. 43, pp. 137–144, Jan. 1995.
[15] W. J. Pierson and L. Moskowitz, "A proposed spectral form of fully developed seas based on the similarity theory of S. A. Kitaigorodskii," *J. Geophys. Res.*, vol. 69, pp. 5181–5203, 1964.
[16] C. L. Rino, T. L. Crystal, A. K. Koide, H. D. Ngo, and H. Guthart, "Numerical simulation of backscatter from linear and nonlinear ocean surface realizations," *Radio Sci.*, vol. 26, pp. 51–71, 1991.
[17] L. Tsang, J. A. Kong, and R. T. Shin, *Theory of Microwave Remote Sensing*. New York: Wiley, 1985.
[18] B. Kinsman, *Wind Waves, Their Generation and Propagation on the Ocean Surface*. Englewood Cliffs, NJ: Prentice-Hall, 1991.
[19] L. B. Wetzel, "Sea clutter," in *Radar Handbook*, M. Skolnik, Ed. New York: McGraw-Hill, 1990.
[20] W. C. Jakes, *Microwave Mobile Communications*. Piscataway, NJ: IEEE Press, 1974.
[21] M. I. Skolnik, *Introduction to Radar Systems*. New York: McGraw-Hill, 1980.
[22] P. Beckmann and A. Spizzichino, *The Scattering of Electromagnetic Waves from Rough Surfaces*. New York: Pergamon, 1963.
[23] D. M. Milder and H. T. Sharp, "An improved formalism for rough surface scattering II: Numerical trials in three dimensions," *J. Acoust. Soc. Amer.*, vol. 91, pp. 2620–2626, 1992.
[24] E. I. Thorsos, "The validity of the Kirchhoff approximation for rough surface scattering using a gaussian roughness spectrum," *J. Acoust. Soc. Amer.*, vol. 83, pp. 78–92, 1988.
[25] ——, "Acoustic scattering from Pierson-Moskowitz sea surfaces," *J. Acoust. Soc. Amer.*, vol. 88, pp. 335–349, 1990.

Baran U. Ungan received the B.S. degree in electrical and electronics engineering from the Middle East Technical University, Ankara, Turkey, in 1996, and the M.S. degree from The Ohio State University (OSU), Columbus, in 1998.

He is currently a Graduate Research Associate with the Department of Electrical Engineering and ElectroScience Laboratory, OSU. His research interests are microwave remote sensing and propagation.

Joel T. Johnson (M'96) received the B.S. degree in electrical engineering from the Georgia Institute of Technology, Atlanta, in 1991, and the S.M. and Ph.D. degrees from the Massachusetts Institute of Technology, Cambridge, in 1993 and 1996, respectively.

He is currently an Assistant Professor with the Department of Electrical Engineering and ElectroScience Laboratory, The Ohio State University (OSU), Columbus. His research interests are in the areas of microwave remote sensing, propagation, and electromagnetic wave theory.

Dr. Johnson is an associate member of Commissions B and F of the International Union of Radio Science (URSI) and a member of Tau Beta Pi, Eta Kappa Nu, and Phi Kappa Phi. He received the 1993 best paper award from the IEEE Geoscience and Remote Sensing Society and was named an Office of Naval Research Young Investigator, National Science Foundation Career awardee, and PECASE award recipient in 1997.